A&A 640, A53 (2020)
https://doi.org/10.1051/0004-6361/202038023

Astronomy & Astrophysics

Saturation mechanism and generated viscosity in gravito-turbulent accretion disks

L. Löhnert[1], S. Krätschmer[2], and A. G. Peeters[1]

[1] Physics Department of Bayreuth, Universitätsstraße 30, Bayreuth, Germany
e-mail: lucas.loehnert@uni-bayreuth.de
[2] Alfred Wegener Institute, Helmholtz Centre for Polar and Marine Research, Bremerhaven, Germany

Received 25 March 2020 / Accepted 6 June 2020

ABSTRACT

Here, we address the turbulent dynamics of the gravitational instability in accretion disks, retaining both radiative cooling and irradiation. Due to radiative cooling, the disk is unstable for all values of the Toomre parameter, and an accurate estimate of the maximum growth rate is derived analytically. A detailed study of the turbulent spectra shows a rapid decay with an azimuthal wave number stronger than k_y^{-3}, whereas the spectrum is more broad in the radial direction and shows a scaling in the range k_x^{-3} to k_x^{-2}. The radial component of the radial velocity profile consists of a superposition of shocks of different heights, and is similar to that found in Burgers' turbulence. Assuming saturation occurs through nonlinear wave steepening leading to shock formation, we developed a mixing-length model in which the typical length scale is related to the average radial distance between shocks. Furthermore, since the numerical simulations show that linear drive is necessary in order to sustain turbulence, we used the growth rate of the most unstable mode to estimate the typical timescale. The mixing-length model that was obtained agrees well with numerical simulations. The model gives an analytic expression for the turbulent viscosity as a function of the Toomre parameter and cooling time. It predicts that relevant values of $\alpha = 10^{-3}$ can be obtained in disks that have a Toomre parameter as high as $Q \approx 10$.

Key words. accretion, accretion disks – protoplanetary disks – hydrodynamics – instabilities – turbulence

1. Introduction

Self-gravity in accretion disks can lead to gravitational instability (GI), which was originally studied in the context of galaxies (Toomre 1964; Lin & Shu 1964; Lynden-Bell & Kalnajs 1972), but is relevant also for accretion disks around young stellar objects and protoplanetary disks (YSOs; PPDs) (Gammie 2001; Kratter & Lodato 2016). The gravitational instability sets in when the Toomre parameter,

$$Q = \frac{c_s \kappa}{\pi G \Sigma}, \tag{1}$$

is smaller than one ($Q < 1$) (Toomre 1964). Here, c_s is the sound speed, Σ is the mass surface density, and κ is the epicyclic frequency, or the angular frequency ($\kappa = \Omega_0$) in the case of a Keplerian disk. The Toomre parameter expresses that a higher temperature (or equivalently a higher sound speed) will stabilize the disk, whereas a higher surface density (Σ) has a destabilizing effect (Kratter & Lodato 2016; Lin & Kratter 2016). Additional physics has been considered since the original derivation, and it has been shown that radiative cooling and viscosity can destabilize the disk for $Q > 1$ (Lin & Kratter 2016).

Numerical simulations have clarified some aspects of the nonlinear evolution of the gravitational instability. In the case of sufficiently fast cooling, fragmentation occurs (Johnson & Gammie 2003; Rice et al. 2003, 2005; Kratter & Murray-Clay 2011; Booth & Clarke 2019), which may be relevant for the formation of massive exoplanets. If the cooling is less efficient, a gravito-turbulent state is obtained, in which the radiation losses are compensated by the heating of the disk through dissipation in shocks (Gammie 2001; Kratter & Lodato 2016). Hence, cooling strongly effects the nonlinear saturation of the gravitational instability (Cossins et al. 2009), and different implementations of the cooling prescription have been tested. These include the so-called β cooling prescription (Gammie 2001), an irradiated version of this latter model (Rice et al. 2011; Baehr & Klahr 2015), and also the solution of the full radiative transfer problem (Hirose & Shi 2019).

One major quality of gravito-turbulence is its ability to transport angular momentum, leading to accretion. A common measure for the angular momentum transport through turbulence is the α-parameter (Shakura & Sunyaev 1973). In a stationary state, the turbulent dissipation connected with the effective viscosity described by the α parameter is then balanced by the energy loss through radiation ($\langle U \rangle / \tau_c$, where τ_c is the cooling timescale on which the thermal energy is lost), yielding (Gammie 2001; Rice et al. 2011)

$$\alpha \approx \frac{4}{9\gamma(\gamma - 1)\tau_c \Omega_0} \left(1 - \frac{U_0}{\langle U \rangle}\right), \tag{2}$$

where γ is the adiabatic index, U_0 the stationary energy density obtained in the absence of turbulence through the combination of irradiation and radiation loss, and $\langle U \rangle$ is the averaged energy density in the presence of turbulence. Although the relation above is a powerful restriction on α, it does not allow a direct prediction because the averaged energy density $\langle U \rangle$ is not a priori known. As $U_0/\langle U \rangle \approx Q_0^2/\langle Q \rangle^2$, a prediction of α is possible when the Toomre parameter of the saturated turbulent state ($\langle Q \rangle$) is known. It is generally accepted that saturation occurs close to marginal stability $\langle Q \rangle \approx 1$ (Kratter & Lodato 2016). However, simulations suggest saturated values higher than one ($1 \lesssim \langle Q \rangle \lesssim 2$) (Rice et al. 2011; Vanon 2018), and those are often associated to the effects of nonaxisymmetric instabilities (Kratter & Lodato 2016; Vanon & Ogilvie 2016; Vanon 2018).

The goal of this paper is to study the nonlinear gravito-turbulent state, and to develop an analytic prediction for $\langle Q\rangle$ and α in the case of an irradiated disk. In Sect. 2 the basic model equations and assumptions used for the study are outlined. Section 3 presents a linear stability analysis, and Sect. 4 gives a short overview of the numerical tool *DiskFlow* including certain benchmarks. Section 5 analyses the nonlinear state, after which the analytic model based on a mixing length approach is introduced in Sect. 6. Section 7 derives some predictions of the analytic model, and conclusions are drawn in Sect. 8.

2. The model

The evolution of the disk is described with the local two-dimensional shearing sheet approximation (Goldreich & Lynden-Bell 1965; Balbus & Hawley 1998; Gammie 2001). The model equations consist of the continuity equation, Euler's equation, the evolution equation for the internal energy density (U), and a Poisson equation for the gravitational potential (Φ) due to the mass density in the disk:

$$\partial_t\Sigma + \nabla\cdot(\Sigma\boldsymbol{v}) = 0 \tag{3a}$$

$$\partial_t\boldsymbol{v} + (\boldsymbol{v}\cdot\nabla)\,\boldsymbol{v} = -\frac{1}{\Sigma}\nabla P - 2\boldsymbol{\Omega}_0\times\boldsymbol{v} + 3\Omega_0^2 x\boldsymbol{e}_x - \nabla\Phi \tag{3b}$$

$$\partial_t U + (\boldsymbol{v}\cdot\nabla)\,U = -\gamma U\,(\nabla\cdot\boldsymbol{v}) - \frac{U-U_0}{\tau_\mathrm{c}} \tag{3c}$$

$$\nabla^2\Phi = 4\pi G\Sigma\cdot\delta(z). \tag{3d}$$

In the equations above, $\boldsymbol{v}$ is the fluid velocity, G is the gravitational constant, and P is the pressure, with the latter linked to the internal energy density (U) through the equation of state

$$P = (\gamma-1)U. \tag{4}$$

The shearing box coordinates (x, y) used in the equations above represent the radial x and azimuthal y direction. The forces per unit mass on the right hand side of the Euler equation, Eq. (3b), include the pressure gradient and the Coriolis, tidal, and self-gravitational forces in that order. The equilibrium is given by a uniform surface mass density (Σ_0) and uniform internal energy density (U_0). This equilibrium incorporates the shear in the Keplerian velocity profile $\boldsymbol{v}_0 = -3\Omega_0 x\boldsymbol{e}_y/2$, which develops through a balance of the Coriolis ($-2\boldsymbol{\Omega}_0\times\boldsymbol{v}$)) and tidal ($3\Omega_0^2 x\boldsymbol{e}_x$) force.

For consistency with the literature (e.g., Gammie 2001) the adiabatic index is chosen as $\gamma = 2$, which agrees with the two-dimensional nature of the system. A model equation for the internal energy rather than an adiabatic closing relation for the pressure ($P = \mathrm{const.}\cdot\Sigma^\gamma$) is necessary, because the β-cooling prescription to mimic the loss of thermal energy due to radiation (Gammie 2001) is applied. Therein, $\beta = \tau_\mathrm{c}\Omega_0$ is the dimensionless cooling timescale. The cooling term incorporates a fiducial thermal energy density, U_0, that the system would obtain in the absence of turbulence. Here, U_0 is motived by the irradiation of the disk by the young star (see e.g., Rice et al. 2011), which, in combination with the radiation losses from the disk, leads to a floor in the thermal energy density.

The equilibrium values Σ_0 and U_0 also define initial values for the Toomre parameter (Q_0) and sound speed $c_{\mathrm{s},0}$, defined as

$$c_\mathrm{s}^2 = \gamma\frac{P}{\Sigma} = \gamma(\gamma-1)\frac{U}{\Sigma}. \tag{5}$$

3. Linear stability in the presence of cooling

The Toomre stability criterion $Q > 1$ was derived assuming the gas behaves adiabatically or barotropically, and expresses the fact that the gas pressure has a stabilizing effect. It is therefore natural to assume that radiative cooling leads to further destabilization and indeed this has been found (see e.g., Lin & Kratter 2016). As the linear instability plays a role for the nonlinear saturated state, it is investigated in some detail in this section.

The model equations of the previous section are linearised around the equilibrium ($\Sigma_0, U_0, \boldsymbol{v}_0 = -(3/2)\Omega_0 x\boldsymbol{e}_y$), $\Phi = 0$,

$$U = U_0 + \tilde{U}, \tag{6a}$$

$$\Sigma = \Sigma_0 + \tilde{\Sigma}, \tag{6b}$$

$$\boldsymbol{v} = -\frac{3}{2}\Omega_0 x\boldsymbol{e}_y + \tilde{v}_x\boldsymbol{e}_x + \tilde{v}_y\boldsymbol{e}_y, \tag{6c}$$

$$\Phi = \tilde{\Phi}, \tag{6d}$$

whereby the tilde denotes a perturbed quantity. Neglecting all quadratic terms in the perturbations then gives a set of equations for the evolution of the perturbations:

$$\partial_t\tilde{\Sigma} + \Sigma_0\partial_x\tilde{v}_x = 0, \tag{7a}$$

$$\partial_t\tilde{v}_x + \frac{\gamma-1}{\Sigma_0}\partial_x\tilde{U} - 2\Omega_0\tilde{v}_y + \partial_x\tilde{\Phi} = 0, \tag{7b}$$

$$\partial_t\tilde{v}_y + \frac{\Omega_0}{2}\tilde{v}_x = 0, \tag{7c}$$

$$\partial_t\tilde{U} + \gamma U_0\partial_x\tilde{v}_x + \frac{\tilde{U}}{\tau_\mathrm{c}} = 0, \tag{7d}$$

where the perturbations have been assumed to be axisymmetric. Substituting $\tilde{f} = \hat{f}\cdot\exp(gt + ikx)$ for all perturbed quantities (f) yields a set of algebraic equations from which the dispersion relation is obtained:

$$g^2 = -\Omega_0^2 + \frac{2c_{\mathrm{s},0}\Omega_0}{Q_0}k - \frac{c_{\mathrm{s},0}^2\tau_\mathrm{c}g}{1+\tau_\mathrm{c}g}k^2. \tag{8}$$

The dispersion relation is similar to that found by Lin & Kratter (2016). Solutions for the growth rate as function of the wave vector for different values of Q_0 and a normalized cooling time, $\beta \equiv \tau_\mathrm{c}\Omega_0 = 10$, are shown in Fig. 1.

Taking the limit $\beta = \tau_\mathrm{c}\Omega_0 \to \infty$ fully recovers the classical Toomre case with the known stability limit $Q_0 > 1$. However, for finite β it follows from the dispersion relation that unstable modes occur for all values of Q_0. The k domain is divided into two regions, with instability only occurring for $k > Q_0/2$ as larger structures (smaller wave numbers) are stabilized by the Coriolis force. One might expect large wave numbers (small structures) to be stabilized as well because the critical Jeans mass cannot be met. However, the cooling extracts the excess thermal energy that is generated by the compression of the fluid, and exponential growth is obtained on timescales that are sufficiently long for this cooling to be effective. This is expressed in Eq. (8) through the occurrence of $\tau_\mathrm{c}g$ in the stabilizing term connected with the pressure response. Therefore, the observation that the value of the Toomre parameter of the saturated turbulent state is larger than one ($\langle Q\rangle > 1$) does not imply linear stability. Although, it should be mentioned that the instability for Q_0 might sensitively depend on the exact choice of the cooling model (see Lin & Kratter 2016, and the discussion in Sect. 7).

The fastest growing mode can be obtained by taking the partial derivative of the dispersion relation towards k and setting

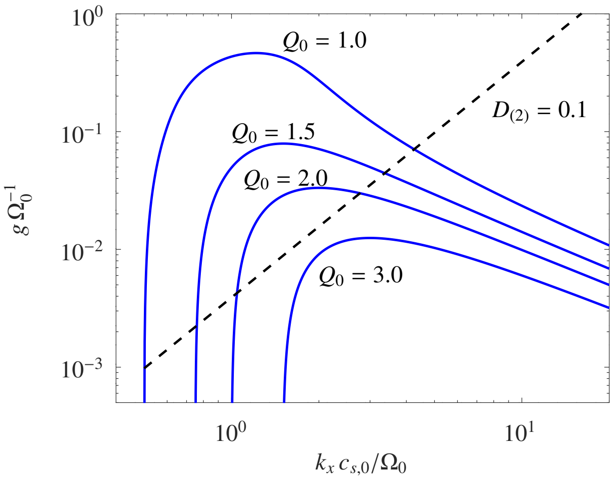

Fig. 1. Linear growth rate g as a function of the radial wave number k_x for different equilibrium Toomre values Q_0 and a cooling time $\beta = \tau_c\Omega_0 = 10$. The straight dotted line gives the damping rate in numerical simulations ($\propto k^2$) for a damping coefficient $D_{(2)} = 0.1$ (see Sect. 4).

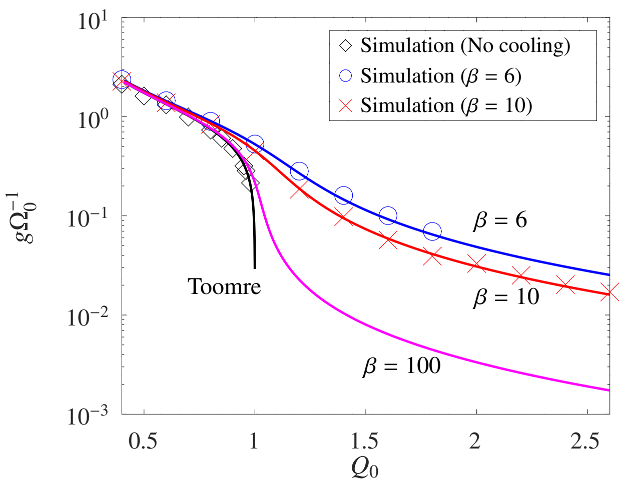

Fig. 2. Analytically obtained growth rates of the most unstable modes, depicted as solid lines. The symbols ∘, ×, and ⋄ correspond to simulations with $\beta = \tau_c\Omega_0 = 6, 10$ and no cooling respectively. The classical Toomre case (no cooling) prevents stability for $Q_0 > 1$. The cooled cases are unstable for all Q_0.

$\partial g/\partial k = 0$ to obtain

$$\frac{k_M c_{s0}}{\Omega_O} = \frac{1+\tau_c g}{Q_0\tau_c g}. \tag{9}$$

Substituting this back into Eq. (8) leads to a cubic polynomial in g only

$$\left(\frac{g}{\Omega_0}\right)^3 - \left(\frac{1}{Q_0^2} - 1\right)\frac{g}{\Omega_0} - \frac{1}{\beta Q_0^2} = 0. \tag{10}$$

Solutions of this equation are shown as solid lines in Fig. 2 for cooling times $\beta \in \{6, 10, 100, \infty\}$. The last case ($\beta \to \infty$) is the classical Toomre criterion without cooling. The analytic expression of the solution $g(k)$ is somewhat extensive, but here the interest is mostly for cases with $Q_0 > 1$ for which the growth rate is relatively small. In this case, the first term in Eq. (10) can be neglected against the second, and one readily obtains

$$\frac{g}{\Omega_0} = \frac{1}{\beta}\frac{1}{Q_0^2 - 1} \qquad \frac{k_M c_{s0}}{\Omega_0} = Q_0, \tag{11}$$

where the maximum wave vector is obtained by inserting the estimate for the growth rate in Eq. (9). The result of Eq. (11) is relatively simple and therefore an easy-to-use estimate of the growth rate that works well for $Q \gtrsim 1.2$. The wave vector is surprising as one usually finds $kc_{s0}/\Omega_0 = 1/Q_0$ according to the classical Toomre criterion in the absence of cooling. The latter is equivalent to a Jeans criterion, stating that for smaller mass densities (larger Q_0) one needs a larger volume (size $\propto 1/k$) to reach the critical mass. In fact, the result in Eq. (11) is assumed to hold for small g. It turns out that for $g\beta >> 1$ one actually finds $kc_{s0}/\Omega_0 = 1/Q_0$ as for the case without cooling. This backs up the above given interpretation that, for a given Q_0, the growth rate is sufficiently small in comparison to $1/\beta$ to allow further collapse.

4. Code and benchmarking

The simulations presented here use the code *DiskFlow*[1] which is a grid-based finite-difference code. The equations solved are the two-dimensional compressible fluid equations outlined above. The fluid equations are integrated using a fourth-order Runge-Kutta method. *DiskFlow* assumes shearing periodic boundary conditions, with the box being periodic in azimuthal y-direction and sheared periodic in the radial x-direction (see e.g., Balbus & Hawley 1998). The Poisson equation for self-gravity is solved using a Fourier transform (Gammie 2001). At each time-step the surface density Σ is transformed to Fourier space $\hat{\Sigma}_{\boldsymbol{k}}$, and the Fourier amplitude of the gravitational potential ($\hat{\Phi}$) is updated through

$$\hat{\Phi}_{\boldsymbol{k}} = -\frac{2\pi G}{k}\hat{\Sigma}_{\boldsymbol{k}}, \tag{12}$$

where $k := |\boldsymbol{k}|$ and $\boldsymbol{k} = (k_x, k_y)$ is the two-dimensional wave vector. The gravitational potential in real space is then obtained through a backward transformation. To avoid difficulties with the Fourier transform in combination with the shearing periodic boundary conditions, a back mapping of the surface mass density, undoing the effect of the shearing and ensuring the solution is periodic in both directions, is performed before the Fourier transform is calculated. Furthermore, a cut-off wave vector $|\boldsymbol{k}|_{\max} = \frac{1}{\sqrt{2}}\min(\frac{\pi N_x}{L_x}, \frac{\pi N_y}{L_y})$ is introduced, following (Gammie 2001). The cut-off acts as a smoothing factor for small-scale gravity. Although this is possibly problematic for cases with clumping (see e.g., Young & Clarke 2015) it has been shown to work well for the gravito-turbulent state.

An artificial viscous pressure is included in *DiskFlow* to guarantee numerical stability

$$P_{\text{vis}} = \zeta\Sigma(\nabla\cdot\boldsymbol{v})^2. \tag{13}$$

This artificial viscous pressure is especially useful in the case of shocks (see e.g., Gammie 2001), as it acts as a viscosity that responds to volumetric changes in the fluid. Moreover, it does not extract energy from the system, as the dissipated kinetic energy is consistently transferred to thermal energy. For the simulations shown here, $\zeta = 0.006$ is chosen.

The code also provides the possibility of using artificial viscosity, which is implemented as a second-order diffusion scheme. More precisely, all of the Eqs. (3a)–(3c) contain an additional dissipative term (second spatial derivatives):

$$\partial_t f + \cdots = \cdots + D_{(2)}(\triangle x)\nabla^2 f, \tag{14}$$

[1] For more details as well as the source code see https://bitbucket.org/astro_bayreuth/accretion-disk-flow/src/master/

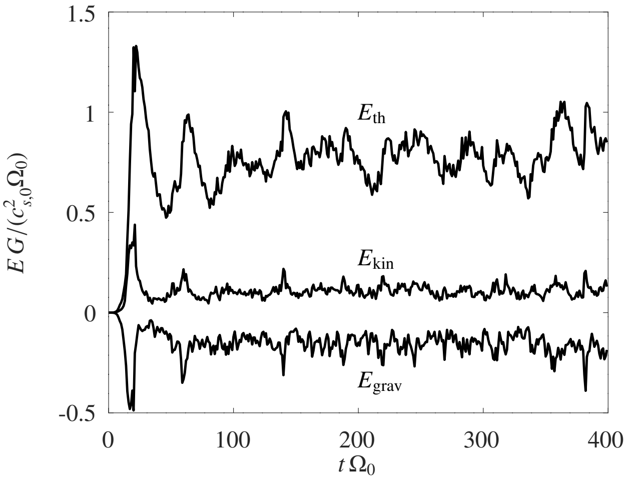

Fig. 3. Temporal evolution of the averaged perturbed energy densities for a simulation with $Q_0 = 1$ and $\beta = 10$. Shown are the mean thermal energy density $E_{\rm th}$, the mean kinetic energy density $E_{\rm kin}$, and the mean gravitational potential energy density $E_{\rm grav}$, as defined in Eq. (16).

with a damping coefficient $D_{(2)}$ and resolution $\triangle x = L/N$. Typical values used for the simulations are $D_{(2)} \sim \{0.07\text{–}0.8\}$. Empirically, it is found that $D_{(2)} \leq 0.1$ is problematic as small-scale perturbations cannot be damped sufficiently and the simulation might eventually become numerically unstable. The coefficient $D_{(2)}$ is made variable in time in order to capture the violent transition from the linear growth phase to the nonlinearly saturated state. In this latter state, the damping coefficient is kept as low as possible. By construction, the damping predominantly acts on small scales (i.e., roughly grid-scale).

All quantities have been made dimensionless using the angular frequency (Ω_0), the sound speed at initialisation (c_{s0}), and the gravitational constant G. With this choice the surface mass density is normalized with $\Sigma_{\rm ch} = c_{s,0}\Omega_0/G$, the internal energy density with $U_{\rm ch} = c_{s,0}^2\Omega_0/G$, and the gravitational potential with $\Phi_{\rm ch} = c_{s,0}^2$. Furthermore, the characteristic length scale $L_{\rm ch} = c_{s,0}/\Omega_0$ is equal to the disk scale height, $L_{\rm ch} = H$, that would be obtained if the vertical force balance were considered. Timescales are normalized with the characteristic time $t_{\rm ch} = \Omega_0^{-1}$, which is consistent with the dimensionless cooling parameter, $\beta \equiv \tau_c\Omega_0$, used before. Unless stated otherwise, all quantities below are dimensionless.

As one of the code benchmarks, the growth rate of the most unstable mode is calculated as a function of the Toomre parameter (Q_0) for different normalized cooling times (β). The numerical results, shown in Fig. 2, are in excellent agreement with the analytic formula obtained in Sect. 3. The simulations use a box size comparable to the analytically derived wavelength of the fastest growing mode and are initialised with random density perturbations. The growth rates are then determined for an interval of exponential growth $t_1 < t < t_2$, using

$$g = \frac{\ln\left(\frac{\langle\tilde{\Sigma}_2^2\rangle}{\langle\tilde{\Sigma}_1^2\rangle}\right)}{2(t_2 - t_1)}. \tag{15}$$

Figure 3 shows that a stationary turbulent state is obtained in the simulations and gives the time evolution of the box-averaged perturbed kinetic, gravitational, and thermal energy densities:

Table 1. Specifications of the example simulation.

Quantity-name	Value
N (grid points)	768
$L_x H^{-1} = L_y H^{-1}$ (box length)	30
Q_0 (Toomre at initialisation)	1.0
$\beta = \tau_c\,\Omega_0$ (cooling time)	10

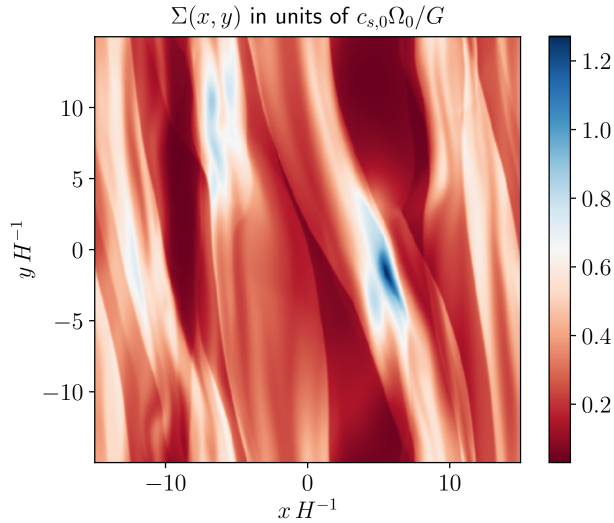

Fig. 4. Snapshot of the surface density $\Sigma(x, y)$ at time $t = 200$ for a simulation with $Q_0 = 1$ and $\beta = 10$.

$$E_{\rm kin} = \frac{1}{2}\langle\Sigma(\tilde{v}_x{}^2 + \tilde{v}_y{}^2)\rangle \tag{16}$$
$$E_{\rm th} = \langle U - U_0\rangle = \langle U\rangle - U_0 = \tilde{U}$$
$$E_{\rm grav} = \frac{1}{2}\langle\Sigma\cdot\phi\rangle.$$

The corresponding simulation parameters are specified in Table 1. The corresponding surface density $\Sigma(x, y)$ and radial velocity $v_x(x, y)$ at $t = 200$ for this simulation are shown in Figs. 4 and 5, respectively. As can be inferred from the images, the system is subject to shock formation. The shocks provide the mechanism for dissipating kinetic energy and to increase the thermal energy which is then lost through radiative cooling.

The α parameter is directly linked to the xy-component of the total stress (S_{xy}). Here, the definition of Ref. (Gammie 2001) is used

$$\alpha = \frac{2\langle S_{xy}\rangle}{3\langle\Sigma c_s^2\rangle} = \frac{2\langle S_{xy}\rangle}{3\gamma(\gamma-1)\langle U\rangle}, \tag{17}$$

where the average $\langle\ldots\rangle$ is over both the simulation domain and time. The total stress consists of the Reynolds and Gravitational stress $S_{xy} = S_{xy}^{(R)} + S_{xy}^{(G)}$, with

$$S_{xy}^{(R)} = \Sigma\,\tilde{v}_x\tilde{v}_y \quad \text{(Reynolds)}, \tag{18}$$
$$S_{xy}^{(G)} = \frac{1}{4\pi}\int_{-\infty}^{\infty}(\partial_x\Phi\cdot\partial_y\Phi)\,\mathrm{d}z \quad \text{(gravitation)}$$
$$= \sum_{\boldsymbol{k}}\frac{k_x\,k_y}{4\pi|\boldsymbol{k}|}|\hat{\Phi}_{\boldsymbol{k}}|^2.$$

(For a derivation of the gravitational stress, see e.g., Lynden-Bell & Kalnajs 1972). A stringent benchmark for the nonlinear

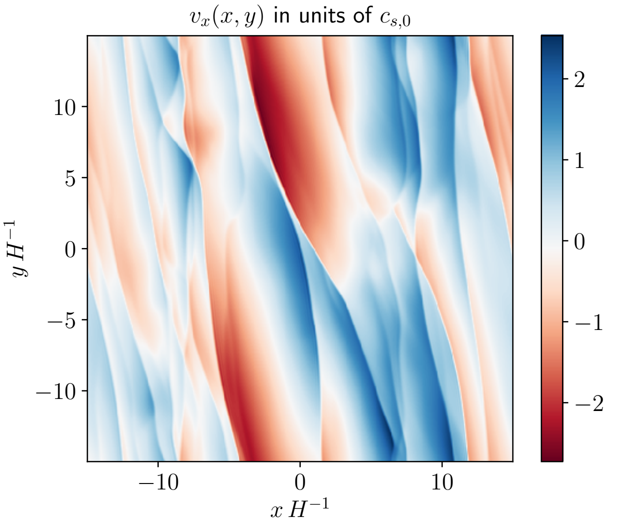

Fig. 5. Snapshot of the radial velocity $v_x(x, y)$ at time $t = 200$ for a simulation with $Q_0 = 1$ and $\beta = 10$.

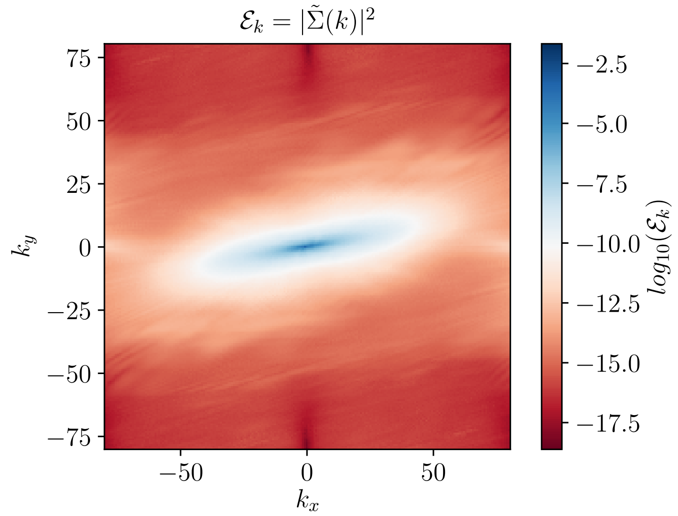

Fig. 7. Two-dimensional power spectrum of the surface density $\mathcal{E}_k(k_x, k_y)$ for the case $Q_0 = 2.2$, $\beta = 10$, $L_x = L_y = 20$, $N = 512$. The image was obtained by averaging all time-snapshots over an interval of orbits $\triangle t = 400$.

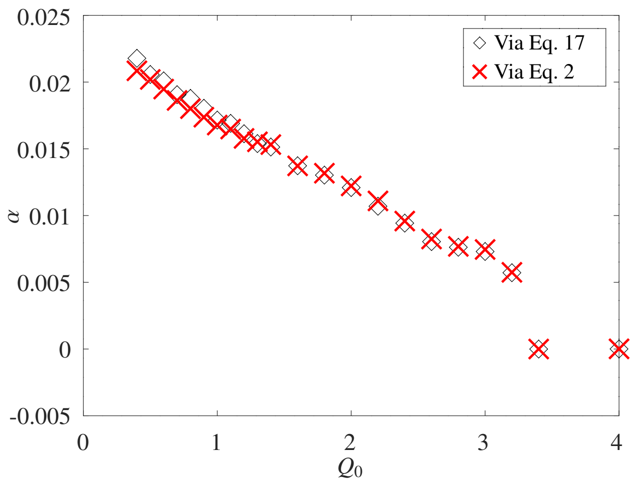

Fig. 6. α-values obtained via two different approaches. Values of α directly obtained from the simulations via averaging of the stresses over both the box and time, according to Eq. (17) ($\diamond$). The values of α were obtained via Eq. (2) ($\times$). All simulations use $\beta = 10$ and the sizes of time averaging intervals are chosen in the range 100−400.

saturated stated is then provided by Eq. (2), which links α to the averaged internal energy $\langle U \rangle$, which can be directly measured in the simulations. The two methods are compared in Fig. 6, which shows that they agree very well. As Eq. (2) is derived from energy conservation, the agreement between the two methods of determining α shows that energy conservation is adequately satisfied numerically.

5. Nonlinear state

To better understand the nature of the gravito-turbulent state, in this section, the nonlinear saturated state is investigated in some detail. Important insights can be obtained through the study of the power spectra in Fourier space. The power spectrum of the perturbed mass surface density $|\hat{\Sigma}(k_x, k_y)|^2$, where $\hat{\Sigma}(k_x, k_y)$ is the Fourier amplitude, is shown in Fig. 7 as a function of the wave vector $\boldsymbol{k} = (k_x, k_y)$. This spectrum is obtained by averaging over a time interval of $\Delta t = 400$ of the fully developed turbulent state. The parameters of the simulation are: $Q_0 = 2.2$ and $\beta = 10$, and a 512×512 grid is used with box sizes $L_x = L_y = 20$. Although the surface mass density spectrum is shown here, the spectrum of the kinetic energy is qualitatively similar.

As can be seen in Fig. 7, the spectrum is not isotropic in the (k_x, k_y) plane. Contours of constant intensity are tilted ellipses, with the spectrum being more extended in the x- than in the y-direction. A similar result has been found Lesur & Longaretti (2011), Mamatsashvili et al. (2014), and Gogichaishvili et al. (2017) for the case of magnetohydrodynamic turbulence. The anisotropy can be explained through the equilibrium flow which sets a unique direction to the system. More specifically, due to the equilibrium shear flow, each structure with a finite k_y develops ever smaller wavelengths in the x-direction or, in other words, the x-component of the wave vector (k_x) is time dependent,

$$k_x = k_{x,0} + \frac{3}{2}\, k_y\, t, \tag{19}$$

(see e.g., Lesur & Longaretti 2011; Goldreich & Lynden-Bell 1965). It has been shown for the case of incompressible magnetohydrodynamic turbulence that the shearing can lead to an anomalous energy transfer in Fourier space in the direction of larger radial wave vectors (Lesur & Longaretti 2011).

In order to study the dependency on k_x (k_y), the spectra are projected onto the k_x (k_y) axis by integrating over k_y (k_x)

$$\mathcal{P}_x \mathcal{E}_k(k_x^{(i)}) \equiv \sum_{j=0}^{N-1} \mathcal{E}_k(k_x^{(i)}, k_y^{(j)}). \tag{20}$$

Depicted in Fig. 8 are the $\mathcal{P}_x$-projections of the power spectra for the kinetic energy density per mass $|\hat{\boldsymbol{v}}(k)|^2$ and the surface density $|\hat{\Sigma}(k)|^2$, for both $Q_0 = 1.2$ and $Q_0 = 2.4$. As expected, the turbulent intensity drops with increasing Q_0. However, the qualitative shape of the spectrum remains unaltered. The spectra appear to obey a scaling law for the range of radial wave numbers $3 \lesssim k_x \lesssim 30$. Depending on whether one studies the surface density or the kinetic energy density per mass, the scaling is between k^{-2} and k^{-3}, as can be seen in Fig. 8. The $\mathcal{P}_y$ projection is shown for comparison in Fig. 9 for an initial Toomre

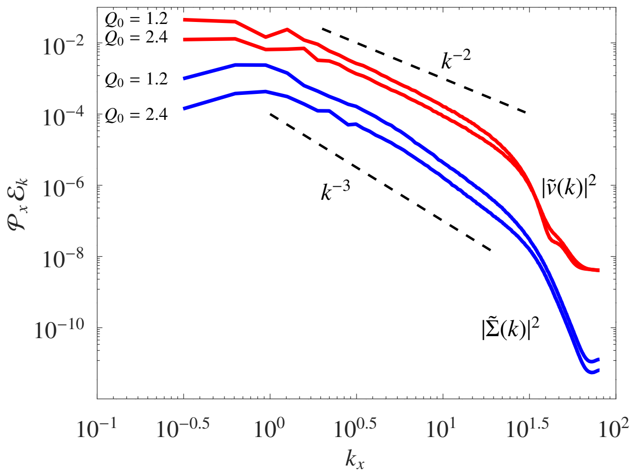

Fig. 8. Projections $\mathcal{P}_x$ of the two-dimensional power spectra onto the k_x-axis for $\mathcal{E}_k = |\hat{v}(k)|^2$ and $\mathcal{E}_k = |\hat{\Sigma}(k)|^2$ respectively. Each of the latter is shown for $Q_0 \in \{1.2, 2.4\}$. Furthermore, the scaling laws k^{-2} and k^{-3} are shown for comparison.

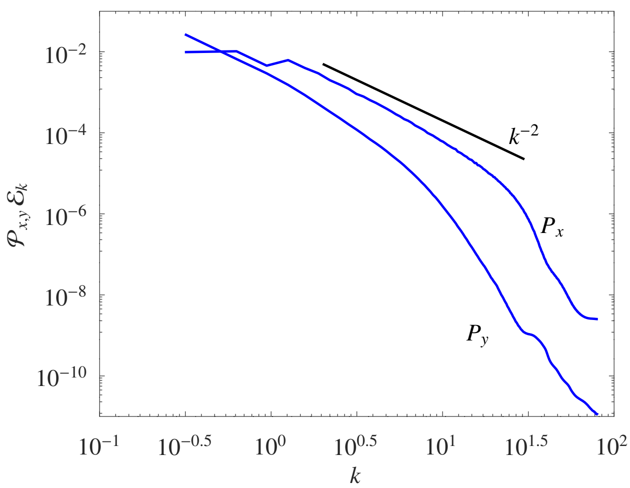

Fig. 9. Projections $\mathcal{P}_x$ and $\mathcal{P}_y$ of the kinetic energy per mass power spectrum onto the k_x and k_y-axis respectively. As can be observed, the $\mathcal{P}_y$-projection drops significantly faster than the $\mathcal{P}_x$-projection. The spectra are shown for $Q_0 = 2.0$.

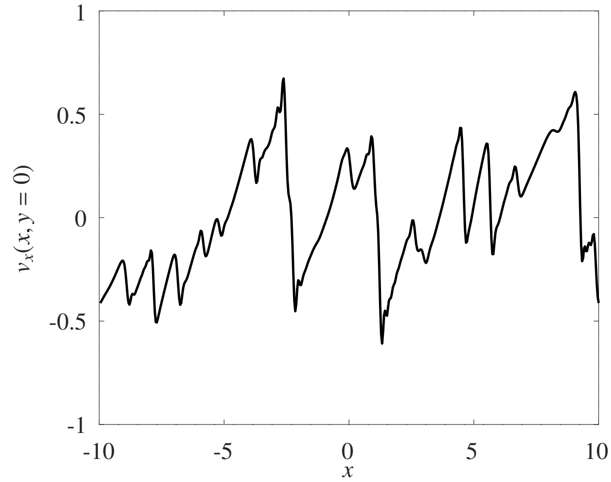

Fig. 10. Slice ($y = 0$) for the radial velocity v_x of a simulation with $Q_0 = 2.8, \beta = 10$. One characteristic of the radial velocity snapshots is the appearance of shocks or velocity discontinuities.

parameter $Q_0 = 2.0$. It can be seen that the projection $\mathcal{P}_y$ drops significantly faster with increasing k_y than $\mathcal{P}_x$ with increasing k_x. The anisotropy therefore increases with increasing wave vectors (we note that the small-scale behavior might differ from that in case of a three-dimensional system (Riols et al. 2017; Booth & Clarke 2019). Furthermore, in contrast to $\mathcal{P}_x$ it is not obvious that $\mathcal{P}_y$ obeys a scaling law.

As the scaling of the x-projections is close to k^{-3}, it is tempting to connect the scaling with the enstrophy cascade of two-dimensional incompressible turbulence (see e.g., Boffetta & Ecke 2012). However, the velocity field of the gravito-turbulence is not incompressible, and in combination with the nonadiabatic response, neither enstrophy nor potential vorticity are conserved. Furthermore, the turbulence is strongly anisotropic. The strong decay of $\mathcal{P}_y\mathcal{E}_k$ with k_y (stronger than k^{-3}) shows that there is no strong cascade in the y-direction. This, together with the increasing anisotropy of the turbulence with increasing wave vector, shows that the velocity nonlinearity, although important, does not completely dominate the dynamics. The gravito-turbulent state is consequently not a strongly turbulent system. At the wave vectors where dissipation becomes important (which can be seen from the change in slope of the spectrum), the energy in the k_y modes is negligible compared to the energy in the k_x modes, and kinetic energy is transferred to internal energy through the dynamics in the radial direction. The wider spectrum in the radial direction is partly due to the shearing that leads to a temporal increase in the radial wave vector given by Eq. (19). However, the scaling of $\mathcal{P}_x\mathcal{E}_k$ with k_x is not entirely consistent with the steep decrease in $\mathcal{P}_y\mathcal{E}_k$ with k_y, when only shearing over a fixed time interval is considered. Additional physics is therefore expected to further broaden the spectrum in the radial direction.

Further insights can be drawn by investigating the radial velocity profiles. Depicted in Fig. 10 is a slice $y = 0$ of the radial velocity $v_x(x, y = 0)$ from a simulation with $Q_0 = 2.8$. The radial velocity in the turbulent state consists of a chaotic superposition of several shocks, where the velocity is discontinuous. These shocks have different widths and heights, and are almost axisymmetric, as can be seen from Fig. 5, reflecting the strong anisotropy in the spectrum. We note that, although the velocity is of the order of the sound speed (i.e., of the order of 1 due to the normalization to the sound speed), almost all the shocks have a step in velocity smaller than the sound speed. Furthermore, at smaller Q_0 the steps are larger and can considerably exceed the sound speed. The shocks that form are not directly due to the Mach number exceeding one in the frame of the computational grid.

The radial profile of the radial velocity is in agreement with the nonlinear wave steepening obtained in Burgers' turbulence (see e.g., Bec & Khanin 2007):

$$\partial_t v_x + v_x \partial_x v_x = 0. \tag{21}$$

An initially unstable sine profile of the radial velocity, $v_x = v_0 \sin(k_x x)$, develops through the nonlinearity with the two adjacent maxima (positive and negative) approaching each other and eventually coalescing. In this process, the original sine profile will change its morphology to a structure similar to those seen in the small image in Fig. 11.

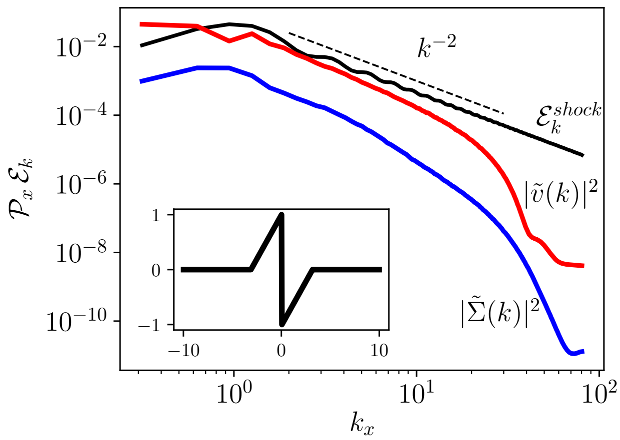

Fig. 11. Comparison of the power spectrum for a single shock $c \cdot |\psi^{\mu}_{\sigma}(k_x)|^2$ with the power spectra for $\mathcal{E}_k = |\hat{\Sigma}(k)|^2$ and $\mathcal{E}_k = |\hat{v}_x(k)|^2$. The shock width is chosen to be $\lambda = 2\pi$ corresponding to $k = 1$ and is depicted in the small subfigure. The constant c is chosen such that the shock spectrum is more comparable to the simulated spectra.

Taking the shock to have a generic form,

$$\Psi^{\mu}_{\lambda}(x) = \begin{cases} \frac{2\mu}{\lambda}(x + \frac{\lambda}{2}) & -\lambda/2 \le x \le 0 \\ \frac{2\mu}{\lambda}(x - \frac{\lambda}{2}) & 0 < x \le \lambda/2 \\ 0 & \text{else,} \end{cases} \tag{22}$$

the Fourier transform can be shown to be

$$\Psi^{\mu}_{\lambda}(k) = i\frac{4\mu}{\lambda}\mathrm{e}^{\mathrm{i}k\,x_0}\frac{1}{k}\left(\frac{\lambda}{2} - \frac{\sin(k\lambda/2)}{k}\right). \tag{23}$$

Therefore, the Fourier spectrum of the shock depicted in Fig. 11 scales as

$$\mathcal{E}^{\text{shock}}_k = f(k_x, \mu, \lambda) \cdot k_x^{-2}, \tag{24}$$

where f modulates the k^{-2} scaling. As the power spectra suggest, most of the energy resides in modes with $k_x \approx 1$. Hence, one might use a width of the shock $\lambda = 2\pi/k \approx 2\pi$. The power spectrum of the shock with this assumption is shown in Fig. 11. The shock spectrum has been scaled vertically for better comparison with the spectra obtained from the simulations. The shock shows a k^{-2} law and the nonlinear spectra of the turbulent state differ only slightly from that scaling. It is noted here that the k^{-2}-scaling is relatively independent of the actual shock width λ and height μ and therefore a chaotic superposition of shocks does not qualitatively alter the appearance of the spectra. Deviations between the shock spectrum and the simulated spectra occur for large values of k_x, suggesting that the deviations are likely due to the artificial viscosity which dominates at larger wave vectors.

The picture that emerges from the studies presented in this section is that the velocity nonlinearity mainly leads to wave steepening in the radial direction. The process continues until a shock forms, with the small radial length scales associated with the shock allowing for efficient dissipation. Modes that are initially growing saturate through the dissipation that occurs when shocks are present.

6. Analytic model

In this section, we develop an analytic model that predicts α for the gravito-turbulent state of an irradiated disk. The model combines a mixing length approach with elements from linear theory. Using the definition of α provided in Eq. (17), and linking the stress to the turbulent viscosity (ν_t) yields

$$\langle S_{xy}\rangle = -\langle\Sigma\rangle\nu_t\frac{\partial\langle v_y\rangle}{\partial x} = \frac{3}{2}\langle\Sigma\rangle\nu_t, \tag{25}$$

where a Keplerian velocity profile in the local approximation $\partial\langle v_y\rangle/\partial x = -3/2$ is used. The kinematic viscosity of the nonlinear state can be estimated using a mixing length approach Shakura (2018). Consider the two dimensional (x, y) shear flow in the local shearing box approximation. A turbulent velocity $\tilde{v}_x$ will move a fluid parcel in the radial direction over a distance δ_x, with the parcel keeping its original y-component of the velocity v_y. Hence, the y-velocity perturbation δv_y is (see Shakura 2018)

$$\delta v_y = \langle v_y\rangle(x) - \langle v_y\rangle(x + \delta_x) \approx -\delta_x\frac{\partial\langle v_y\rangle}{\partial x}. \tag{26}$$

The averaging brackets $\langle\ldots\rangle$ are assumed to be spatial and temporal averages (more technically, one can also assume them to be ensemble averages, see e.g., Shakura 2018). Using the equation above in the stress yields

$$\langle\Sigma v_x\delta v_y\rangle \approx -\langle\Sigma\rangle\cdot\langle\delta_x v_x\rangle\cdot\frac{\partial\langle v_y\rangle}{\partial x}, \tag{27}$$

and comparison with equation (25) then gives the mixing length estimate of the kinematic viscosity

$$\nu_t = \langle\delta_x v_x\rangle = \langle\delta_x^2/\delta_t\rangle, \tag{28}$$

where in the second step the radial velocity is expressed through a typical timescale of $v_x = \delta_x/\delta_t$.

In order to predict α, Eq. (2) is used to eliminate $\langle U\rangle$ in Eq. (17), yielding

$$\alpha = \frac{2}{3\gamma(\gamma-1)}\langle S_{xy}\rangle\frac{1 - \frac{9}{4}\gamma(\gamma-1)\beta\alpha}{U_0}. \tag{29}$$

Subsequently, expressing the stress in the kinematic viscosity using Eq. (25), gives

$$\alpha = \frac{\nu_t}{1 + \frac{9}{4}\gamma(\gamma-1)\beta\nu_t} = \frac{\nu_t}{1 + \frac{\nu_t}{\alpha_0}}, \tag{30}$$

whereby $\alpha_0 \equiv 4/(9\gamma(\gamma-1)\beta)$ is used for the last step. We would like to point out that $\nu_t \neq \alpha$, as ν is normalized with the background sound speed $c_{s,0}$ rather than saturated speed of sound $\langle c_s\rangle$. Using the mixing length model for ν_t in the equation above gives an expression for α.

As discussed in Sect. 5, saturation occurs through the nonlinear steepening of radial waves. Since the maximum (minimum) of the wave has to move over roughly a quarter wavelength to generate the observed shock structures, the mixing length can be taken to be a quarter wavelength of the dominant radial mode:

$$\delta_x = \frac{\lambda}{4} = \frac{\pi}{2}k^{-1}. \tag{31}$$

The spectra of the nonlinear state decrease in amplitude with increasing Q_0, but the functional dependence on k_x remains nearly unaltered. Therefore, the typical wave vector appearing in the mixing length estimate is relatively nonsensitive to the Q_0 value, and a typical value can be obtained by averaging over the spectrum:

$$\langle k_x\rangle_k = \frac{\int|\hat{\Sigma}(k)|^2 k_x\,\mathrm{d}^2\boldsymbol{k}}{\int|\hat{\Sigma}(k)|^2\,\mathrm{d}^2\boldsymbol{k}}. \tag{32}$$

This procedure yields

$$\bar{k} \approx \frac{3}{2} \tag{33}$$

as a typical value for $\bar{k}$. It then follows that $\bar{\lambda} = 2\pi/\bar{k} \approx 4$, which fits with the average distance between two shock fronts in Fig. 5, and agrees with the results of previous work (e.g., Kratter & Lodato 2016; Cossins et al. 2009) showing that dissipation occurs at wave numbers $\bar{k} \approx 1$ through sonic shocks.

The typical timescale can be argued to be linked to the growth rate. Although, for many turbulent systems, linear theory is not particularly relevant, we show in the previous section that the nonlinear state of the gravito-turbulence is not strongly turbulent. The relevance of linear theory can be further justified by the following observations.

– There must be a mechanism providing an ongoing exchange of energy from the background (shear flow) to the actual turbulent motion of the fluid. A linear instability is a candidate for this mechanism. Indeed, the strength of turbulence drops with increasing values of Q_0 as can be seen in Fig. 8 in agreement with the dependence of the linear growth rate g on Q_0.
– The relevance of linear theory for the nonlinear state can be further assessed by investigating cases close to the threshold of the linear instability. With radiative cooling, the disk is analytically unstable for all values of the Toomre parameter. However, due to the added dissipation, this is not necessarily the case in the numerical simulations. This is illustrated in Fig. 6, where it can be seen that for $Q_0 > 3$ the disk is stable when a diffusion coefficient $D_{(2)} = 0.1$ is used. Indeed, numerical simulations with $Q_0 > 3.2$ ($D_{(2)} = 0.1$) show no turbulent state even when initialised with a turbulent state obtained for $Q_0 < 3$. Although there is a window in Q_0 where turbulence can be maintained despite linear stability, at least for some time, this window is small. Therefore, in summary, the development of gravito-turbulence requires a linear instability to be present.

The relevance of the linear drive suggests that the growth rate plays a role in the determination of the typical timescale. Consequently $\delta_t^{-1} = g$ is used as the typical inverse timescale. Using that and Eq. (33), one finds an analytical expression for the turbulent kinematic viscosity:

$$\nu_t = \left(\frac{\pi}{2}\right)^2 \frac{g}{\bar{k}^2} = \left(\frac{\pi}{3}\right)^2 g. \tag{34}$$

We note that something similar is often used in fusion plasma physics in the context of turbulent transport (Weiland 2016).

The analytic result of Eq. (34) can subsequently be used to predict α according to Eq. (30). Indeed, g depends on both the Toomre parameter Q and the cooling timescale β.

7. Predictions of the analytic model

Analytic linear growth rates were obtained for an equilibrium without turbulence and are therefore a function of Q_0. The saturated Toomre parameter of the turbulent state $\langle Q \rangle$, with $\langle ... \rangle$ denoting averages over the computational domain as well as time, is found to be larger than one and close to $\langle Q \rangle \approx 2$ in two-dimensional systems (see e.g., Vanon 2018). The simulations of this paper confirm this observation but nevertheless show that saturation can occur at values considerably larger than 2, and that $\langle Q \rangle$ is a function of irradiation as well as cooling time. The turbulent saturation values obtained from the simulations are depicted as crosses in Fig. 12. The average was calculated in the following way:

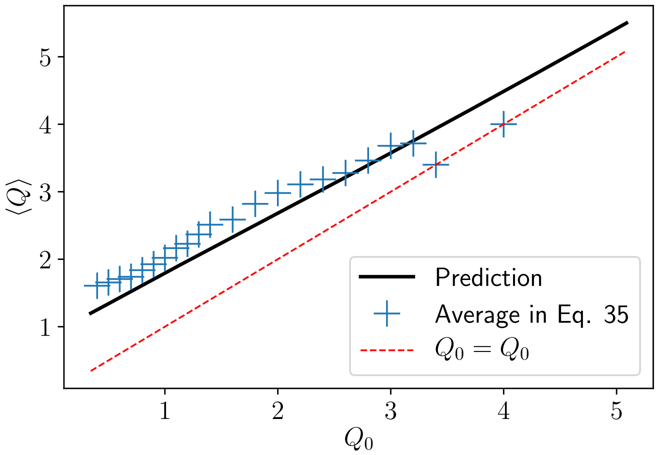

Fig. 12. Toomre parameter at turbulent saturation $\langle Q \rangle$ plotted as a function of irradiation equilibrium Q_0. Crosses: values derived from simulations by averaging the turbulent state over both box and time according to Eq. (35). Solid line: analytical prediction via Eqs. (36) and (37).

$$\langle Q \rangle = \frac{\Omega_0}{\pi G} \sqrt{\frac{\gamma(\gamma-1)\langle U \rangle}{\langle \Sigma \rangle^3}}. \tag{35}$$

The relevant timescale in the mixing length model is set by the linear growth rate. However, the latter must describe the growth in the saturated turbulent state. Consequently, the growth rate must be considered a function of $\langle Q \rangle$ and $\delta_t^{-1} = g(\langle Q \rangle, \beta)$.

As $\langle Q \rangle > 1$, the approximate growth rate from Eq. (11) is used and substituted into Eq. (34):

$$\nu_t = \left(\frac{\pi}{3}\right)^2 \frac{1}{\beta} \frac{1}{\langle Q \rangle^2 - 1} \tag{36}$$

$$\alpha = \frac{\nu_t}{1 + \nu_t/\alpha_0},$$

where $\bar{k} = 3/2$ is used. This latter equation relates α with $\langle Q \rangle$. The prediction is completed using Eq. (2), which provides a relation between α and $\langle U \rangle$ and consequently $\langle Q \rangle$ as well. For the purpose here, it is convenient to rewrite Eq. (2) in terms of ν_t

$$\left(\frac{\langle Q \rangle}{Q_0}\right)^2 = \left(1 - \frac{\alpha}{\alpha_0}\right)^{-1} \tag{37}$$

$$\langle Q \rangle = Q_0 \sqrt{1 + \frac{\nu_t}{\alpha_0}},$$

where $\langle U \rangle / U_0 = \langle Q \rangle^2 / Q_0^2$ is used. Hence, one can now predict both α and $\langle Q \rangle$ depending on the irradiation equilibrium Q_0.

The prediction of $\langle Q \rangle$ as derived above is shown as the black solid line in Fig. 12. One conclusion that can be drawn directly from Eq. (37) is that $\langle Q \rangle > Q_0$ always holds. Furthermore, as $g \to 0$ for $\langle Q \rangle \to \infty$, we conclude that $\langle Q \rangle \to Q_0$ for $Q_0 \to \infty$ by considering Eq. (36). The prediction for α depending on Q_0 is shown in Fig. 13.

The predictions seem to fit the data well except for values of $Q_0 > 3.2$. This discrepancy is due to the above-mentioned numerical damping, which prevents a turbulent state from being sustained as the linear driving is compromised. More precisely, the simulations for $Q_0 = 3.4$ and 4.0 could not maintain a turbulent state. The corresponding values for α and $\langle Q \rangle$ are obtained by averaging the decaying turbulence, in the absence of a persistent nonlinear state.

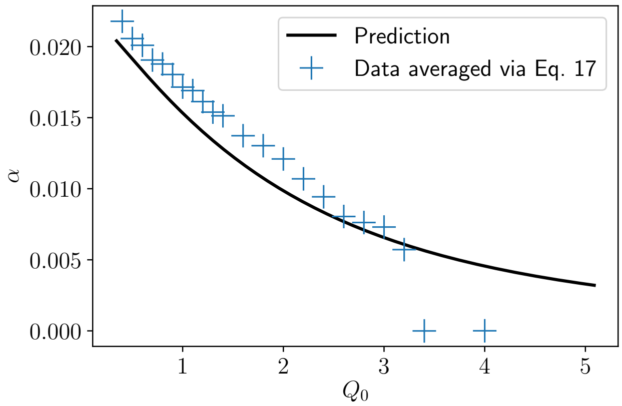

Fig. 13. Comparison of the analytical mixing length prediction with the simulation data. Crosses: α values derived by averaging the simulation data over both box and time according to Eq. (17). Black curve: prediction from the mixing length argument in Eqs. (36) and (37).

We note that the analytic model predicts comparatively large α values for high background Toomre parameters Q_0. To see that, one can approximate Eq. (30) assuming small growth rates,

$$\alpha = \left(\frac{\pi}{3}\right)^2 \frac{1}{\beta} \frac{1}{Q_0^2 - 1}, \tag{38}$$

whereby $\langle Q \rangle \approx Q_0$ for large Q_0. Assuming $\beta = 10$, a relevant value $\alpha = 10^{-3}$ is obtained for $\langle Q \rangle \approx 10$, that is, an order of magnitude above the Toomre stability criterion. Of course, shorter cooling times lead to larger values of α at fixed $\langle Q \rangle$. However, shorter cooling may also lead to clumping (Johnson & Gammie 2003; Rice et al. 2003, 2005, 2011; Kratter & Murray-Clay 2011). The effects of clumping are beyond the scope of this work but a study of this effect at the higher values of $\langle Q \rangle$ obtained in this paper when compared with the literature is worthy of further study.

It is noted that the prediction of $\alpha > 10^{-3}$ for $\langle Q \rangle \approx 10$ is connected with the stability analysis in Sect. 3. The latter might depend on the cooling model that is applied. Here, the fiducial cooling level is a constant background thermal energy density U_0. Alternatively, one can choose the reference cooling level to be density dependent, leading to a cooling term (Rice et al. 2011)

$$-\frac{\Sigma(c_s^2 - c_{s0}^2)}{\gamma(\gamma-1)\tau_c} = -\frac{U}{\tau_c} + \frac{\Sigma c_s^2}{\gamma(\gamma-1)\tau_c}. \tag{39}$$

Linearization leads to an additional term $\propto \tilde{\Sigma}$ (see e.g., Lin & Kratter 2016), when compared with the analysis of Sect. 3. This additional term has stabilizing effects as locally compressed areas are cooled less efficiently than locally expanding areas. Indeed, linear stability analysis reveals that the cooling model presented in Eq. (39) yields positive growth rates only for $Q_0 < \sqrt{\gamma}$ or in the case discussed here: $Q_0 \lesssim 1.4$. Nevertheless, the β-cooling description is a strong simplification and one could argue for both cooling models. To fully elucidate the problem, one would have to solve the full radiative transfer equation.

8. Conclusion

In this paper, the gravito-turbulent state of a razor-thin irradiated disk is studied in detail. We show that, depending on the cooling prescription, a linear instability occurs for all values of the equilibrium Toomre parameter Q_0, and we derive an accurate analytic estimate of the maximum growth rate for $Q_0 > 1$. A detailed study of the spectra reveals that the gravito-turbulent state is not strongly turbulent. The spectra are anisotropic with the anisotropy increasing with the wave vector. The spectra drop off rapidly with k_y (stronger than k_y^{-3}) and show no clear power-law scaling with k_y. This suggests that no cascade in the y-direction takes place and saturation is connected with dynamics in the radial direction. In contrast, the spectrum as a function of the radial wave vector does show a power law with a scaling in the range $k^{-2} - k^{-3}$, which can be explained through the existence of shocks. The radial velocity profile as a function of the radial coordinate is consistent with Burgers' turbulence, consisting of several shocks of different height. The observations suggest that linearly unstable modes grow in amplitude until the nonlinearity is strong enough, leading to wave steepening and shock formation. The small radial scales connected with the shock then allow for efficient dissipation and, consequently, saturation of the mode.

Using these observations, a mixing length model is developed using a quarter wave length as the radial step length and the growth rate of the most unstable mode as the typical time. This model gives an analytic prediction of the viscosity parameter α as a function of the Toomre parameter and cooling time, and it compares very well with the numerical simulations. The model predicts relevant values of $\alpha = 10^{-3}$ for Toomre parameters an order of magnitude larger than the original Toomre limit (i.e., $\langle Q \rangle \approx 10$). It is noted that this result can change when using a different cooling description and more accurate models with radiative transfer would be useful here.

References

Baehr, H., & Klahr, H. 2015, ApJ, 814, 155
Balbus, S. A., & Hawley, J. F. 1998, Rev. Mod. Phys., 70, 1
Bec, J., & Khanin, K. 2007, Phys. Rep., 447, 1
Boffetta, G., & Ecke, R. E. 2012, Ann. Rev. Fluid Mech., 44, 427
Booth, R. A., & Clarke, C. J. 2019, MNRAS, 483, 3718
Cossins, P., Lodato, G., & Clarke, C. J. 2009, MNRAS, 393, 1157
Gammie, C. F. 2001, ApJ, 553, 174
Gogichaishvili, D., Mamatsashvili, G., Horton, W., Chagelishvili, G., & Bodo, G. 2017, ApJ, 845, 70
Goldreich, P., & Lynden-Bell, D. 1965, MNRAS, 130, 125
Hirose, S., & Shi, J.-M. 2019, MNRAS, 485, 266
Johnson, B. M., & Gammie, C. F. 2003, ApJ, 597, 131
Kratter, K., & Lodato, G. 2016, ARA&A, 54, 271
Kratter, K. M., & Murray-Clay, R. A. 2011, ApJ, 740, 1
Lesur, G., & Longaretti, P.-Y. 2011, A&A, 528, A17
Lin, C., & Shu, F. 1964, ApJ, 140, 646
Lin, M.-K., & Kratter, K. M. 2016, ApJ, 824, 91
Lynden-Bell, D., & Kalnajs, A. J. 1972, MNRAS, 157, 1
Mamatsashvili, G. R., Gogichaishvili, D. Z., Chagelishvili, G. D., & Horton, W. 2014, Phys. Rev. E, 89, 043101
Rice, W. K. M., Armitage, P. J., Bate, M. R., & Bonnell, I. A. 2003, MNRAS, 339, 1025
Rice, W. K. M., Lodato, G., & Armitage, P. J. 2005, MNRAS, 364, L56
Rice, W. K. M., Armitage, P. J., Mamatsashvili, G. R., Lodato, G., & Clarke, C. J. 2011, MNRAS, 418, 1356
Riols, A., Latter, H., & Paardekooper, S.-J. 2017, MNRAS, 471, 317
Shakura, N. 2018, Accretion Flows in Astrophysics, Astrophys. Space Sci. Libr., 454 (Springer)
Shakura, N. I., & Sunyaev, R. A. 1973, A&A, 24, 337
Toomre, A. 1964, ApJ, 139, 1217
Vanon, R. 2018, MNRAS, 477, 3683
Vanon, R., & Ogilvie, G. I. 2016, MNRAS, 463, 3725
Weiland, J. 2016, Plasma Phys. Rep., 42, 502
Young, M. D., & Clarke, C. J. 2015, MNRAS, 451, 3987